

Effect of Nb doping on the structural, morphological, optical and electrical properties of RF magnetron sputtered In_2O_3 nanostructured films

R. Reshmi Krishnan¹, S. R. Chalana¹, S. Suresh¹, S. K. Sudheer¹, C. Sudarsanakumar², M. C. Santhosh Kumar³, and V. P. Mahadevan Pillai^{*1}

¹ Department of Optoelectronics, University of Kerala, Thiruvananthapuram 695581, Kerala, India

² School of Pure and Applied Physics, Mahatma Gandhi University, Priyadarsini Hills, Kottayam 686560, Kerala, India

³ Optoelectronic Materials and Devices Lab, Department of Physics, National Institute of Technology, Tiruchirappalli 620015, India

Received 4 June 2016, revised 13 September 2016, accepted 11 October 2016

Published online 4 November 2016

Keywords indium oxide, Nb, doping, photoluminescence, spectroscopic ellipsometry

* Corresponding author: e-mail vpmpillai9@gmail.com, Phone: +04 712308167

Undoped and niobium (Nb) doped indium oxide (In_2O_3) thin films are prepared by radio frequency magnetron sputtering technique. The effect of Nb on the structural, morphological, optical and electrical properties of In_2O_3 films are analyzed using techniques such as X-ray diffraction (XRD), micro-Raman spectroscopy, X-ray photoelectron spectroscopy, atomic force microscopy, field emission scanning electron microscopy (FESEM), energy dispersive X-ray spectroscopy, UV–visible spectroscopy, spectroscopic ellipsometry, photoluminescence spectroscopy and Hall effect measurements. XRD analysis reveals that the as-deposited undoped and Nb doped films are polycrystalline in nature with cubic bixbyite

structure. Raman analysis supports the presence of cubic bixbyite structure of In_2O_3 in the films. XPS analysis shows a decrease of oxygen deficiency due to Nb and the existence of Nb as Nb^{4+} in the In_2O_3 lattice. The band gap energy of the films increases with increase in Nb concentration. PL spectra reveal intense UV and visible emissions in all the films. Optical constants of the films are determined using spectroscopic ellipsometry. The thickness of films estimated using FESEM and ellipsometry are in good agreement. The carrier concentration, mobility and nature of carriers are measured using Hall measurement technique in Van der Pauw configuration at room temperature.

© 2016 WILEY-VCH Verlag GmbH & Co. KGaA, Weinheim

1 Introduction Over the years, investigations have been carried out extensively on transparent conducting oxides (TCOs) owing to their diverse technological applications [1–3]. Among the TCOs, indium oxide (In_2O_3) has attracted great interest due to its wide band gap (direct band gap energy of 3.5–3.75 eV) [4], chemical inertness and good adherence to the substrate [5]. In_2O_3 is an insulator in its stoichiometric form and becomes conducting when it is non-stoichiometric [6]. In_2O_3 thin films have wide range of applications including transparent windows in liquid crystal displays [7, 8], solar cells [9], electrochromic devices [10], optoelectronic devices [11], gas sensors [12, 13] and nanoelectronic building blocks [14]. The optical and electrical properties of In_2O_3 show strong dependence on de-

fect density produced by external doping or disturbed stoichiometry as well as their preparation and growth conditions [15]. Doping In_2O_3 by transition elements with high carrier mobility such as Mo, Ti, W and Nb can improve the optical and electronic properties considerably [16–21]. Niobium (Nb) can be a dopant for In_2O_3 because the substitution of Nb^{5+} ions into In^{3+} sites can produce more electrons which can enhance the conductivity in Nb-doped In_2O_3 films. Since the ionic radius of Nb^{5+} ions (0.064 nm) [22] is smaller than that of In^{3+} ions (0.080 nm) [23], the doping of Nb^{5+} ions in In^{3+} site can result in lattice deformation [24]. There are only few reports on Nb in In_2O_3 [21, 24–28]. Earlier reports show that Nb-doped In_2O_3 thin films possess high values of transparency, conductivity and mobility.

Co-sputtered Nb doped In_2O_3 films are used as transparent anodes for organic solar cells by Kim et al. [24]. Nb-doped In_2O_3 thin films with high values of conductivity, mobility and transparency were prepared by laser ablation by Gupta et al. [25, 26]. Lozano et al. [27, 28] studied the effect of Nb doping concentration in In_2O_3 lattice at a substrate temperature of 550 °C using a co-sputtering system. Nb-doped In_2O_3 thin films were prepared by sol-gel spin coating technique by Mohammadi et al. [21]. The objective of this study is to investigate the effect of Nb on the structural, morphological, optical and electrical properties of In_2O_3 thin films prepared by RF magnetron sputtering technique.

2 Experimental Nb doped In_2O_3 films were prepared by RF magnetron sputtering technique. A mixture of In_2O_3 powder (Sigma Aldrich 99.99% purity) and Nb_2O_5 powder (Sigma Aldrich 99.99% purity) with different doping concentrations viz., 0, 1, 2, 3, 5 and 7 wt% was well grinded and pressed powder was used as targets for sputtering. The deposition chamber was first evacuated to a pressure of 3×10^{-6} mbar and pure argon gas was admitted (at a pressure of 0.015 mbar) into the chamber. The deposition of the films was done on cleaned quartz substrates (kept at a distance of 5 cm from the target) using an RF power of 120 W for a duration of 40 minutes. The as-deposited films with different Nb concentrations namely 0, 1, 2, 3, 5 and 7 wt% were designated as N0, N1, N2, N3, N5 and N7, respectively, and were used for structural, electrical and optical characterization.

The structural properties of the as-deposited films were investigated by X-ray diffraction (Bruker AXS D8 Advance) measurements employing $\text{Cu K}\alpha_1$ radiation with a wavelength of 1.5406 Å in the 2θ range 20°–70° at a scan rate of 0.02° per minute in the Bragg Brentano geometry. Micro-Raman spectra of the films were recorded using Labram-HR 800 spectrometer (Horiba Jobin Yvon) equipped with Synapse CCD camera system maintained at -70 °C using an excitation radiation at wavelength 514.5 nm from an argon ion laser at a spectral resolution of about 1 cm^{-1} . The chemical composition of the films were investigated using X-ray photoelectron spectrometer (XPS) (Omicron Technology) with monochromatic $\text{Al K}\alpha$ (1486.7 eV) X ray source. The XPS data analysis was done using the CASA XPS software. The surface morphology of the films was characterized using atomic force microscope (Bruker-Dimension edge with Scan Asyst) in contact mode and field emission scanning electron microscope (Nova Nano SEM-450, FEI, USA) equipped with XFlash detector 6/10 (Bruker). The elemental analysis of the films was done using electron energy dispersive X-ray spectrometer (EDS-Quantax 200, Germany). Optical transmittance and reflectance spectra over the wavelength range of 200–900 nm of the films were recorded using a UV-Visible (JASCO, V-550) double beam spectrophotometer. Thin film parameters such as thickness, refractive index, extinction coefficient and dielectric constant of Nb doped In_2O_3 films were

determined in the wavelength range 450–825 nm using spectroscopic ellipsometer (Horiba Jobin Yvon MM-16). The thickness of the films was also estimated from the cross-sectional FESEM images. The electrical resistivity, mobility, carrier type and carrier concentration of the thin films were measured at room temperature using Hall measurement (ECOPIA-HMS5000) technique in van der Pauw configuration. Room temperature photoluminescence spectra of the films were recorded using Fluoromax-4 spectrophotometer equipped with 150 W xenon lamp.

3 Results and discussion

3.1 XRD analysis Figure 1 shows the XRD patterns of as-deposited Nb doped In_2O_3 films. The XRD pattern of the pure In_2O_3 film shows an intense peak at $2\theta = 30.59^\circ$, two less intense peaks at 2θ values 21.47° and 51.01° and two weak peaks at 2θ values 41.76° and 45.86°. These peaks can be attributed to lattice reflection planes (222), (211), (440), (332) and (431), respectively of cubic bixbyite structure of indium oxide [JCPDS File no. 71-2195]. In the film with 1 wt% Nb (N1), an appreciable enhancement in the intensity of the peaks can be seen which can be attributed to the enhancement in crystallinity with Nb doping. In the films with higher Nb concentration, the intensity of the peaks decreases, showing the reduction of crystallinity at higher Nb concentrations. But the XRD intensity of film N3 shows a slight enhancement compared to film N2 which might be due to the higher thickness of N3 film. A regular increase in full width at half maximum (FWHM) of the (222) peak with increase in Nb concentration is observed which can be attributed to the stress introduced in the film due to Nb doping. The orientation of the grains in specific crystallographic directions is related with minimization of free surface energy density of the film and the energy density of the interface between the film and substrate [29]. From the high intensity of the (222) peak, it can be seen that $\langle 111 \rangle$ is the preferred direction of crystal growth in all these films. The (222) plane is a close packed plane in In_2O_3 cubic bixbyite structure with lowest surface energy [30].

The relative intensities of peaks corresponding to different lattice reflection planes obtained for different films with that of the powder diffraction database (JCPDS File no. 71-2195) are calculated and shown in Fig. 2. A high degree of randomness for the peaks can be seen for the different films. The ratio of intensity of the most intense peak (222) to the intensity of other peaks is estimated for different films and the values obtained are shown in Table 1. In the XRD pattern of all the films, (222) peak remains as the highest intense peak and (440) peak is the second highest intense peak. A systematic decrease of I_{222}/I_{440} ratio with increase in Nb concentration upto 5 wt% can be seen in Table 1. For the N7 film this ratio shows a slightly higher value compared to N5 film. The decrease of I_{222}/I_{440} ratio with increase in Nb concentration can be an indication of the change in the preferred orientation of crystalline

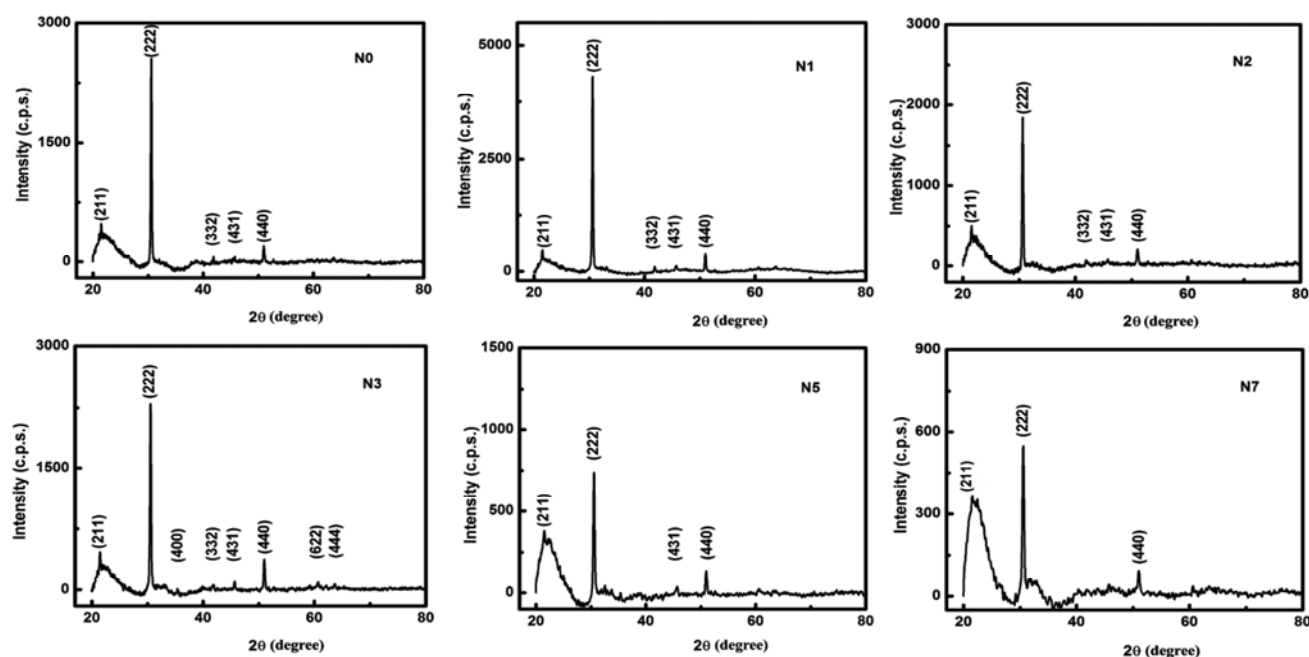


Figure 1 XRD patterns of as-deposited undoped and Nb₂O₅ doped In₂O₃ films deposited by RF magnetron sputtering technique on quartz substrate with RF power of 120 W.

growth with Nb. However the value of I_{222}/I_{440} ratio is higher for both the undoped and Nb doped films compared to that obtained for In₂O₃ powder (JCPDS File no. 71-2195).

The average size (D) of the crystallites in the films is determined using Scherrer formula [32]

$$D_{hkl} = \frac{0.9\lambda}{\beta \cos \theta}, \quad (1)$$

where λ is the wavelength of the X-ray, θ is the Bragg diffraction angle and β is the FWHM in radians. The average size of the crystallites is estimated using the data for the most intense peak (222). A systematic reduction in the size of the crystallites with increase in Nb concentration is observed (Table 2) and this indicates that Nb hinders the growth of the In₂O₃ grains [21].

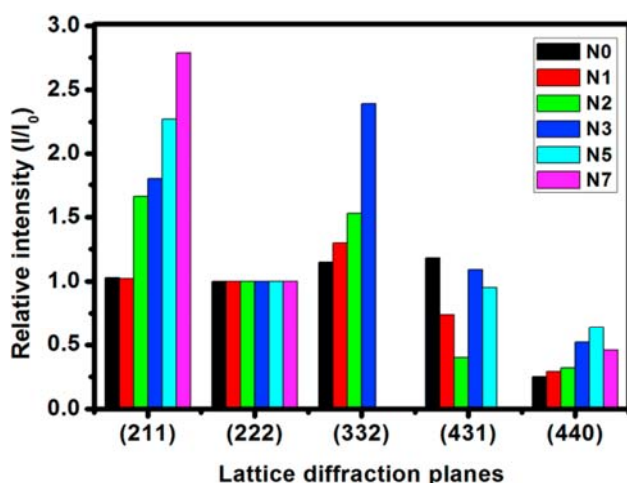


Figure 2 Intensity comparison of various peaks with corresponding peaks of powder data diffraction obtained for different films.

The reported value of the lattice constant a for bulk In₂O₃ crystal is 1.0118 nm [31]. The lattice constant calculated for all the films (Table 2) is in agreement with the reported value.

Table 1 Relative intensities of different XRD peaks for undoped and Nb doped films.

Relative intensity	N0	N1	N2	N3	N5	N7	In ₂ O ₃ powder*
I_{222}/I_{440}	12.7	10.8	9.7	6.1	4.9	5.9	3.1
I_{222}/I_{211}	16.0	16.0	9.9	9.1	7.2	6.8	16.4
I_{222}/I_{431}	21.2	34.0	-	19.01	26.5	-	25.0
I_{222}/I_{332}	39.7	35.0	29.7	22.9	-	-	45.5

*JCPDS File no. 71-2195.

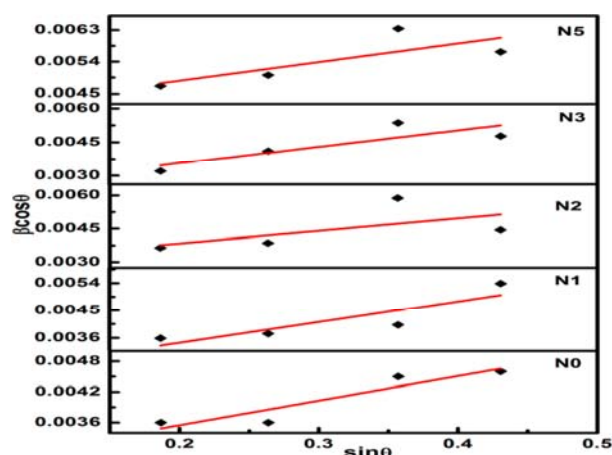


Figure 3 Williamson-Hall plot for as-deposited undoped and Nb doped In_2O_3 films deposited by RF magnetron sputtering technique on quartz substrate.

The effect of crystallite size and strain induced broadening in the FWHM of XRD peak can be studied by Williamson-Hall plot (W-H plot) using the relation [33]:

$$\beta \cos \theta = \frac{k\lambda}{D'} + 2\eta \sin \theta, \quad (2)$$

where D' is the actual particle size, k is the correction shape factor which can be taken as 0.9 for spherical grains, and η is the residual strain.

The corresponding values of β and θ for the XRD peaks with significant intensities in the XRD patterns are used for plotting the W-H plot. From the W-H plot (Fig. 3), strain free crystallite size and strain in the films are calculated (Table 2). It can be seen that the size of the crystallites calculated from the W-H plot is higher than that calculated from Scherrer formula for all the films. This indicates that there is strain induced broadening of the XRD peaks in all the films.

3.2 Micro-Raman analysis In_2O_3 having bcc bixbyite structure belongs to the space group Ia3 with 8 formula units per Bravais unit cell. Four In atoms occupy S_6 site, 12 In atoms occupy C_2 site and 24 oxygen atoms occupy the general site C_1 .

The group theoretical analysis, under the factor group T_h using Fateley et al. [34], yields 117 optical modes at $k = 0$, the centre of the Brillouin zone and are distributed as [35]

$$\Gamma_{\text{opt}} = 4A_g(R) + 4E_g(R) + 14F_g(R) + 5A_u + 5E_u + 16F_u(IR) \quad (3)$$

where A_g and F_g modes are Raman active only, while the F_u modes are infrared active only. The A_u and E_u modes are inactive in both Raman and infrared spectra.

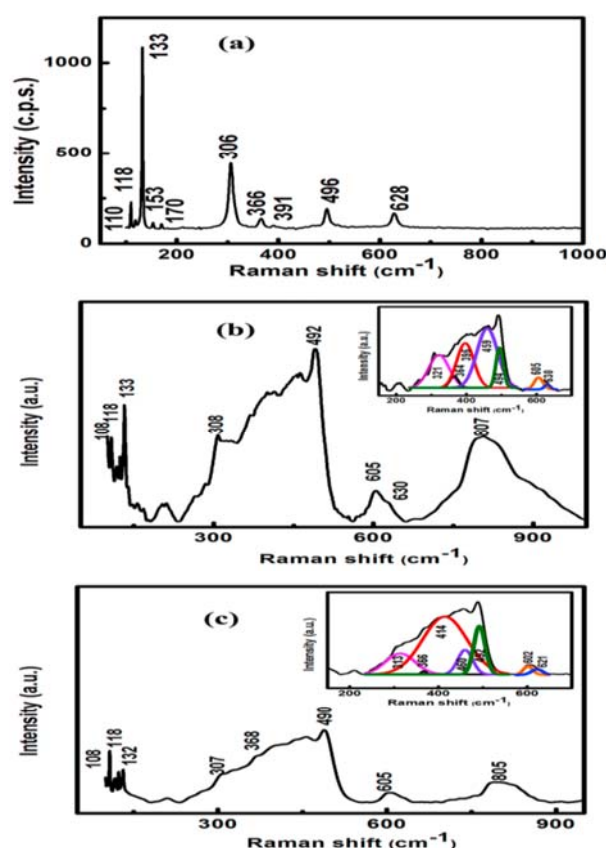


Figure 4 Micro-Raman spectra of (a) In_2O_3 powder, (b) undoped In_2O_3 film N0 and (c) 1 wt% Nb doped In_2O_3 film N1. Deconvoluted spectra in the wave number range 215–630 cm^{-1} are given as inset in the Raman spectra.

The micro-Raman spectra of the undoped and Nb doped In_2O_3 films are recorded. Figure 4 presents the micro-Raman spectra of the In_2O_3 powder, as-deposited undoped and 1 wt% Nb doped In_2O_3 films. The deconvoluted spectra of the wave number region 235–660 cm^{-1} are shown in the inset of the Raman spectra of the films. The intense Raman band at $\sim 133 \text{ cm}^{-1}$ can be assigned to the stretching vibration of In-O bond of InO_6 structural unit [36]. A broad band $\sim 308 \text{ cm}^{-1}$ obtained in the Raman spectra of all the films can be attributed to the bending vibration of InO_6 octahedron [36, 37]. In the Raman spectra of the films, the weak band at 369 cm^{-1} can be assigned to the stretching vibrations of In-O-In bridge and is an indication of the presence of oxygen vacancies in the structure [36]. The bands ~ 492 and 630 cm^{-1} can be attributed to the stretching vibrations of InO_6 [13, 37]. The bands $\sim 807 \text{ cm}^{-1}$ obtained in the Raman spectra of the films may be due to the spectral contribution from the quartz substrate [38].

3.3 XPS analysis The surface composition and elemental chemical states of the Nb doped films are analyzed by X-ray photoelectron spectroscopy. Figure 5(a) and 5(b) depicts the XPS survey spectra of the N0 and N7 films scanned from 0 to 1000 eV. The survey spectrum of the

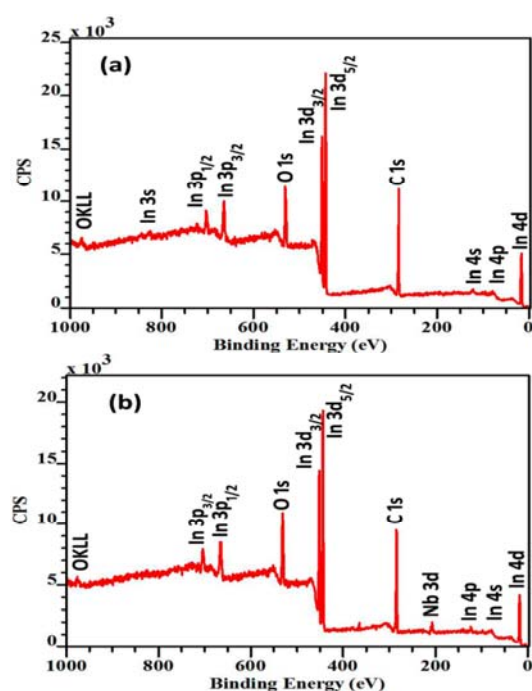


Figure 5 XPS survey spectra of (a) undoped film N0 and (b) 7 wt% Nb doped In_2O_3 film N7 deposited on quartz substrate by RF magnetron sputtering technique.

film N0 shows peaks of indium, oxygen and carbon whereas the survey spectrum of the Nb doped film (N7) shows the peaks associated with Nb in addition to these elements. As the films get exposed to the atmosphere, they have a detectable quantity of adventitious carbon contamination. The binding energy of all the spectra is calibrated with reference to the $\text{In } 3d_{3/2}$ peak [39].

Figure 6(a) and 6(c) shows the $\text{In } 3d$ core level spectra of the undoped film N0 and 7 wt% doped film N7. Gaussian fitting of the $\text{In } 3d$ region in the films N0 and N7

shows double peaks with a spin–orbit splitting of ~ 7.6 eV. For the film N0, the two peaks are observed at binding energies 443.97 eV and 451.56 eV which can be attributed to the $\text{In } 3d_{5/2}$ and $\text{In } 3d_{3/2}$ peaks of In_2O_3 [40, 41]. For the film N7, these peaks are observed at 444.31 eV and 452.05 eV respectively.

The observation of double peaks in the oxygen 1s spectra is common for oxides containing cations with multiple valence states [42, 43]. Banger et al. [44] fitted the oxygen 1s peak to a superposition of three Gaussian components with positions centred at ~ 530 , 531 and 532 eV reflecting three different oxygen environments. They attributed the binding energy peak at 530 eV to lattice oxygen atoms in a fully-coordinated environment, the peak at 531 eV to oxygen atoms in the vicinity of an oxygen vacancy and the higher binding energy peak at 532 eV to M–OH (M-metal) species. The O 1s core level spectra of the films N0 and N7 are shown in Fig. 6(b) and 6(d), respectively. Gaussian fitting of the O 1s spectra shows two peaks at 529.07 eV (O_I) and 530.97 (O_{II}) eV for the film N0. These peaks are observed at 529.49 eV (O_I) and 531.20 eV (O_{II}) for the film N7. The low binding energy O_I peak for the undoped film N0 corresponds to In_2O_3 lattice oxygen atoms [45]. For the film N7, O_I peak at 529.49 eV can be assigned to the oxygen (O^{2-}) anion in In_2O_3 or Nb-oxides [46]. Naeem et al. [47] attributed the high binding energy peak at 531.6 eV to O^{2-} ions in the oxygen deficient region. Luhan et al. [48] assigned the photoelectron line with a binding energy 531.9 eV to the surface adsorbed oxygen in various forms as well as to the oxygen incorporated in a hydroxyl group. Hence the higher energy peaks observed at 530.97 eV for N0 film and at 531.20 eV for N7 film can be due to O^{2-} ions in the oxygen deficient region or to the surface adsorbed oxygen.

Table 2 Structural and morphological parameters of as-deposited Nb_2O_5 doped In_2O_3 films by RF magnetron sputtering technique.

Sample code	FWHM (degree)	Lattice constant a (nm)	Average crystallite size (nm)		Lattice strain from W-H plot	Film thickness (nm)		Root mean square value of surface roughness (nm)
			From Scherrer formula	From W-H plot		Using FESEM	Using ellipsometric analysis	
N0	0.213	1.0115	39	53 \pm 07	0.0023	230	228.75 \pm 0.39	2.03
N1	0.222	1.0110	37	54 \pm 15	0.0026	216	212.67 \pm 0.45	2.69
N2	0.244	1.0092	34	51 \pm 20	0.0028	225	217.78 \pm 0.30	2.09
N3	0.244	1.0124	34	51 \pm 16	0.0026	270	266.78 \pm 0.71	1.47
N5	0.298	1.0122	28	38 \pm 07	0.0028	200	193.20 \pm 1.11	2.60
N7	0.288	1.0122	29	-	-	195	191.83 \pm 0.28	1.19

Table 3 XPS data: Binding energy, relative strengths of indium and oxygen components and peak ratio ($\text{O}_{\text{II}}/\text{O}_{\text{total}}$) of undoped film (N0) and 7 wt% Nb doped In_2O_3 film (N7).

Sample code	Positions (eV)				Relative strengths (%)				Peak ratio ($\text{O}_{\text{II}}/\text{O}_{\text{total}}$)
	O_{I}	O_{II}	$\text{In}3d_{5/2}$	$\text{In}3d_{3/2}$	O_{I}	O_{II}	In_{444}	In_{452}	
N0	529.07	530.97	443.97	451.56	22.06	77.94	60.98	39.02	0.779
N7	529.49	531.20	444.31	451.89	22.54	77.66	60.15	39.85	0.776

The core level spectra of Nb 3d in the film N7 is shown in Fig. 6(e). Deconvolution of the Nb 3d peak using CASAXPS software yields two components with medium intense peaks at binding energies 206.44 eV and 209.20 eV. These peaks observed with a spin orbit splitting of 2.76 eV can be attributed to the Nb $3d_{5/2}$ and Nb $3d_{3/2}$ peaks of Nb^{4+} [28]. This shows the presence of an oxygen deficient phase in the Nb doped film. Table 3 summarizes the peak positions and relative strengths of In and O. It is observed from Table 3 that In 3d and O 1s peaks of the film N7 is shifted towards higher binding energy. The intensity ratio of $\text{O}_{\text{II}}/\text{O}_{\text{total}}$ for films N0 and N7 is ~ 0.78 . The

electronegativity difference between Nb (1.6) and O (3.44) is larger than that between In (1.78) and O (3.44) [49]. Due to the higher Nb-O bond strength, the higher will be the probability of capturing oxygen atoms during the deposition, and hence the lower oxygen deficiency concentration.

4 Surface morphology

4.1 AFM analysis The surface morphology and surface roughness of the films are examined using AFM. The 3D AFM images of as-deposited Nb doped In_2O_3 films on a scan area 500 nm x 500 nm is shown in Fig. 7. The AFM images of the films present a uniform dense distribution of

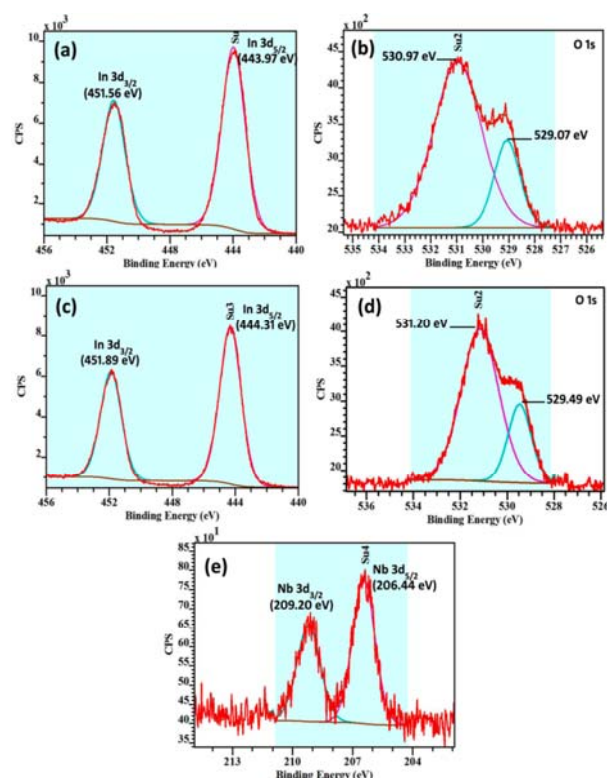


Figure 6 (a) In 3d core level spectra of undoped film N0, (b) O 1s core level spectra of film N0, (c) In 3d core level spectra of 7 wt% Nb doped film N7, (d) O 1s core level spectra of film N7 and (e) Nb 3d core level spectra of 7 wt% Nb doped film N7 deposited on quartz substrate by RF magnetron sputtering technique.

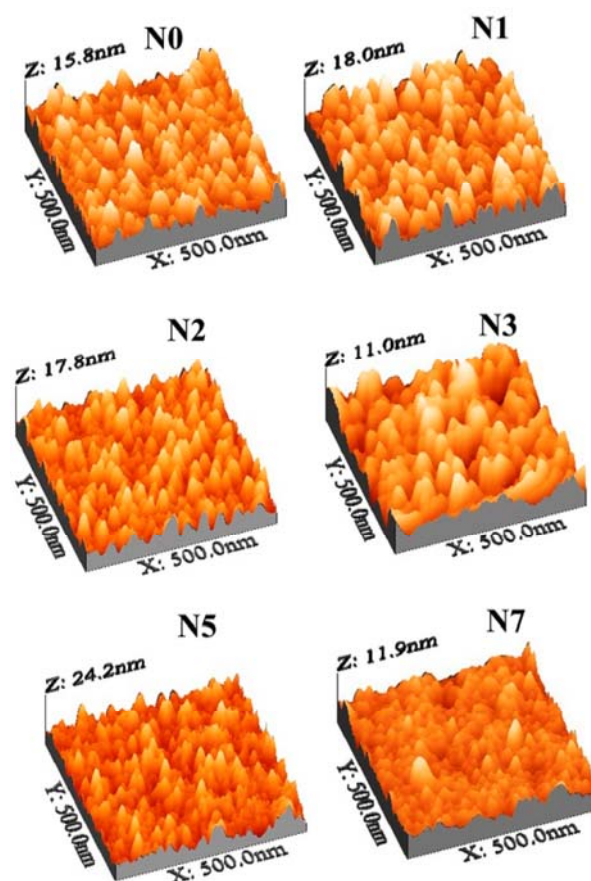


Figure 7 3D AFM images of as-deposited undoped and Nb doped In_2O_3 films deposited by RF magnetron sputtering technique on quartz substrate for various wt% of Nb.

well-defined grains with good grain boundary. This indicates the good crystalline nature of the film as evidenced from the XRD analysis. The film with 7 wt% Nb shows a tendency of agglomeration of grains. The root mean square surface roughness (rms) of the films is obtained using WSxM 5.0 Develop 6.4 software [50]. All the films present low values for rms surface roughness (Table 2) indicating a smooth morphology.

4.2 FESEM and EDS analysis The surface morphology of the films is also analyzed using FESEM analysis. Figure 8 shows the FESEM images of undoped and Nb doped In_2O_3 films deposited by RF magnetron sputtering technique. As revealed by the AFM analysis, the FESEM images also support a smooth surface morphology for both undoped and doped films. The FESEM images of all the films show a uniform dense distribution of smaller grains. The elemental analysis of the undoped and doped films is done by EDS analysis. The typical EDS spectra of two films N0 and N7 are shown in Fig. 9(a) and 9(b), respectively. The observation of Nb peaks supports the incorporation of Nb in the doped films. A systematic increase of incorporation of Nb with increase in doping concentration can be seen in Fig. 9(c).

The cross-sectional FESEM images of as-deposited Nb doped In_2O_3 films are shown in Fig. 10. The thickness of the films estimated from these images is given in Table 2.

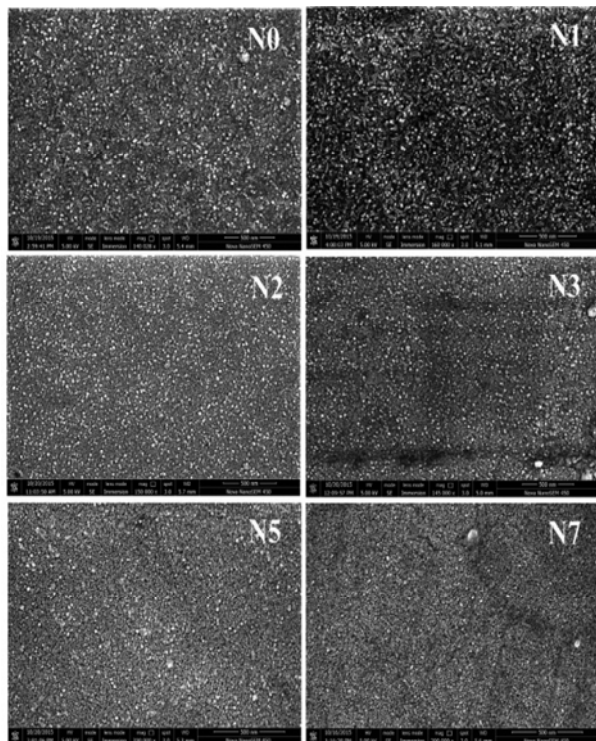


Figure 8 FESEM images of as-deposited undoped and Nb doped In_2O_3 films deposited by RF magnetron sputtering technique on quartz substrate.

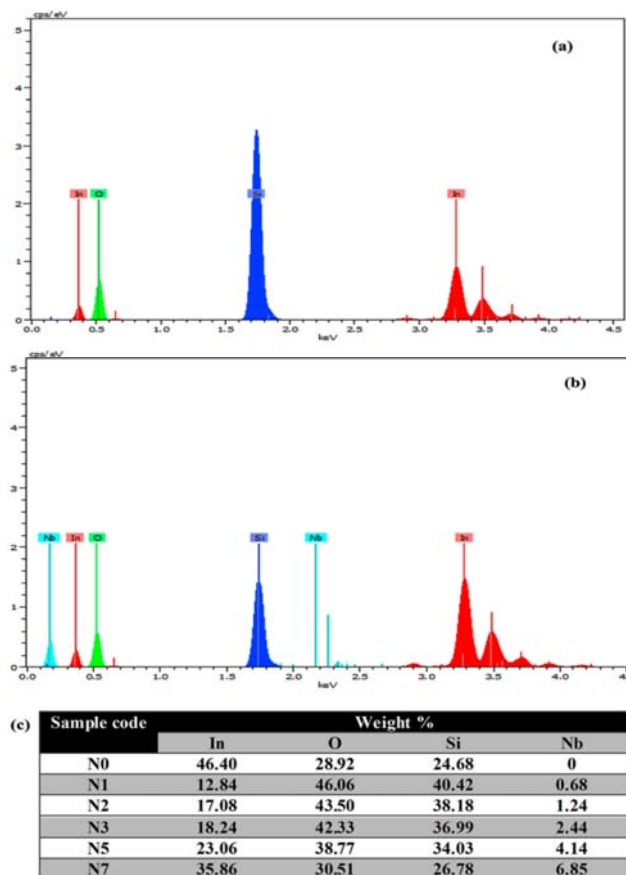


Figure 9 EDS spectra of as-deposited (a) undoped film N0 and (b) 7 wt% Nb doped In_2O_3 film N7 and (c) percentage of elements in the films obtained from EDS analysis.

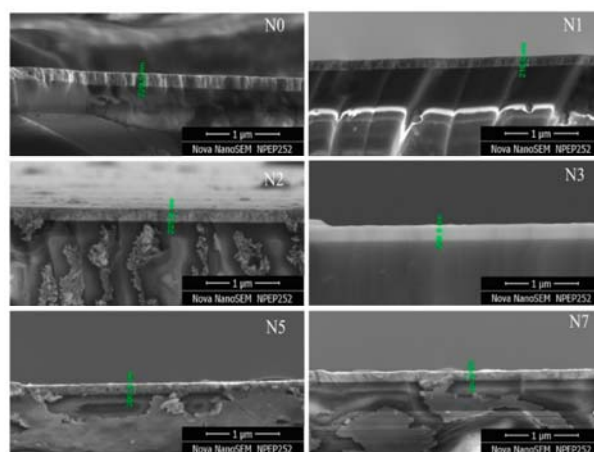


Figure 10 Cross-sectional FESEM images of the as-deposited undoped and Nb doped In_2O_3 films deposited on quartz substrate by RF magnetron sputtering technique showing the thickness.

The film N3 shows the highest thickness among the Nb doped In_2O_3 films. The cross sectional FESEM images show the formation of film of uniform thickness on the substrate.

5 Optical analysis

5.1 UV-visible analysis The degree of transparency and band gap of the films are determined from the optical measurements. The transmittance and reflectance spectra of as-deposited undoped and Nb doped In_2O_3 films are shown in Fig. 11(a) and 11(b), respectively.

Average transmittance of the films in the wavelength range 400–900 nm are calculated and given in Table 4. All the films show very high transmittance in this region (81–86%). The high transparency of the films can be due to their good crystalline quality and smooth surface morphology. A smooth and uniform surface morphology reduces scattering loss. All the films show a sharp decrease in transmittance below 400 nm region due to the fundamental absorption edge of In_2O_3 . Almost a systematic blue shift of fundamental absorption edge with increase in Nb concentration can be seen in the transmittance spectra. The oscillations observed in the transmittance and reflectance spectra of the films can be due to the interference of light arising from the difference in refractive indices of the film and substrate and multiple reflections at the two film edges i.e., film/air and film/substrate interface [51, 52]. These oscillations give an evidence of homogeneous films with a smooth and uniform film surface as evident from AFM and FESEM analysis.

The absorption coefficient α at different wavelengths is calculated using the following relation:

$$\alpha = \frac{1}{t} \left[\ln \frac{(1-R)^2}{T} \right], \quad (4)$$

where t is the film thickness, R is the reflectance and T is the transmittance of the film.

The band gap energy E_g can be estimated from the following relation [53]:

$$\alpha(h\nu) = A(h\nu - E_g)^n, \quad (5)$$

where α is the absorption coefficient, the constant A is the band edge sharpness which is related with the order in crystalline structure of deposited films, n is the Planck's constant, ν is the frequency of radiation, E_g is the band gap corresponding to a particular transition occurring in the film, and the exponent n characterizes the nature of band transition which can take values $1/2$, $3/2$, 2 or 3 depending on whether the transitions are direct allowed, direct forbidden, indirect allowed and indirect forbidden transitions respectively [53, 54].

The plot of α^2 versus photon energy ($h\nu$) of as-deposited undoped and Nb doped In_2O_3 films is shown in Fig. 11(c). It is observed that for all the films, the best straight line is obtained for $n = 1/2$ indicating direct allow-

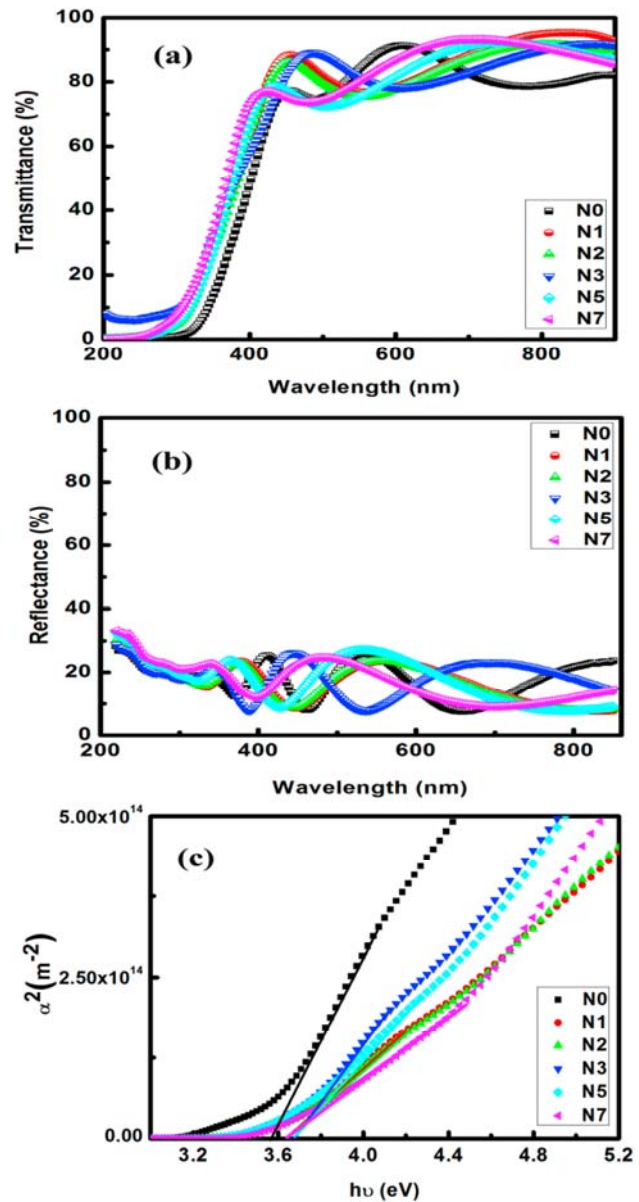


Figure 11 (a) Transmittance spectra and (b) reflectance spectra and (c) α^2 versus $h\nu$ plot of as-deposited undoped and Nb doped In_2O_3 films deposited on quartz substrate by RF magnetron sputtering technique.

ed transition in these films. The band gap is determined for all the films from the plot of $(\alpha)^{1/n}$ versus photon energy $h\nu$ on the x-axis by extrapolating the linear region of the graph to $h\nu = 0$. The band gap energy estimated for undoped In_2O_3 film is 3.56 eV. The Nb doped In_2O_3 films present a higher value of band gap energy compared to that of the undoped film.

A systematic increase of band gap energy with increase in Nb concentration upto 5 wt% Nb concentration is observed (3.56–3.69 eV); thereafter the band gap energy slightly decreases (3.65 eV). The shift in band gap energy may arise from several factors such as improvement or re-

duction in crystallinity, quantum size effect, change in the density of impurities, tensile or compressive strain in the films etc. [55]. XRD analysis shows a reduction in crystallite size with Nb doping. The XPS analysis reveals that Nb-doped film is oxygen deficient. Thus, the observed shift in band gap energy with Nb doping can be due to the reduction in crystallite size and to oxygen deficiency concentration [56] in the films.

5.2 Spectroscopic ellipsometry analysis The optical constants being closely related to the electronic polarizability of ions and the local field inside materials play an important role in the design of optical devices and optical communication [57]. The optical constants of the Nb doped In_2O_3 films are determined using spectroscopic ellipsometry at room temperature. For measuring the ellipsometric parameters psi (Ψ) and delta (Δ), transmittance spectra of all the films deposited on quartz substrate are measured using Horiba Jobin Yvon MM-16 ellipsometer. The Ψ and Δ spectra are acquired at an angle of incidence of 70° in the wavelength range 450–825 nm (2.75–1.50 eV). Optical modelling and data analysis are done using the DELTAPSI2TM software [58]. The ellipsometric data of the undoped and Nb doped In_2O_3 films are analysed by a three layer model of the samples as given in Fig. 12(a). The surface layer consists of In_2O_3 : Nb and voids and the middle layer is bulk In_2O_3 : Nb layer.

The thickness and optical constants of the bulk layer are determined using a classical oscillator dispersion relation containing a single oscillator and a Drude term [59].

$$\varepsilon_\infty = \varepsilon'_\infty + \frac{(\varepsilon_s - \varepsilon'_\infty)\omega_t^2}{\omega_t^2 - \omega^2 + i\Gamma_0\omega} + \frac{\omega_p^2}{-\omega^2 + i\Gamma_D\omega}, \quad (6)$$

where ε_∞ is the high frequency dielectric constant, ε_s is the strength of oscillator, ω_t the frequency and Γ_0 the damping factor of the oscillator. ω_p and Γ_D are the frequency and damping factor related to the plasma term respectively.

The experimental and model Ψ and Δ spectra for the films with different Nb concentrations are shown in Fig. 12(b)–(g). The quality of fit is estimated by the value of mean square deviation (χ^2). In the present case, the value of χ^2 is less than 1 for all the films (Table 4) indicating the best fit between experimental and calculated data.

Figure 13(a)–(d), respectively, shows the variation of refractive index (n), extinction coefficient (κ), real and imaginary parts of dielectric constant (ε_r and ε_i , respectively) of the Nb doped In_2O_3 films as a function of wavelength. The refractive index of all the films shows a systematic decrease with increase in wavelength showing normal dispersion behaviour. The rate of decrease of refractive index with wavelength is higher at shorter wavelengths (i.e. near the fundamental absorption edge) than at the longer wavelengths.

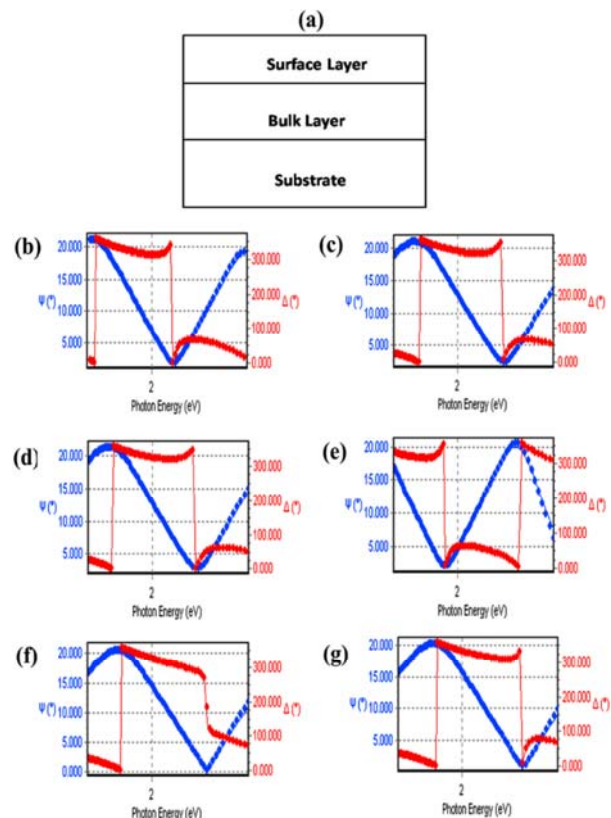


Figure 12 (a) Stack model of the Nb doped In_2O_3 thin film sample for ellipsometry data analysis. Ψ and Δ spectra at an angle of incidence of 70° for (b) N0, (c) N1, (d) N2, (e) N3, (f) N5, and (g) N7 films. Solid curves represent experimental data and dotted curves represent best fit model data.

The refractive index of the films for a typical wavelength 550 nm is calculated and shown in Table 4. The values of refractive index for the films lie in the range 2.02–2.14 and are in good agreement with the reported values for In_2O_3 films [60, 61]. Among the Nb doped films, the film N5 has the highest value of refractive index. The extinction coefficient (κ) of all the films shows a decrease with increase of wavelength. For films of high doping concentration, the rate of decrease of κ with wavelength is larger for shorter wavelengths compared to that of longer wavelengths. The low value of extinction coefficient indicates very low optical losses due to absorption leading to high transparency of the films in the wavelength range considered which is consistent with the transmission spectra obtained for the films (Fig. 11(a)).

The variation of ε_r and ε_i with wavelength decreases with increase in wavelength. It is observed from Fig. 13(c) and 13(d), the value of the real part of dielectric constant ε_r is greater than the imaginary part ε_i . The variation of ε_r with wavelength and the variation of n with wavelength follow similar pattern for all films. The variation of ε_i with wavelength and the variation of extinction coefficient κ with wavelength follow a similar pattern for all films.

The complex dielectric constant can be calculated by the following relation [62, 63]

$$\tilde{\epsilon}(h\nu) = \epsilon_r(h\nu) - i\epsilon_i(h\nu) \quad (7)$$

where ϵ_r and ϵ_i are the real and imaginary parts of dielectric constant, respectively.

Loss factor is calculated using the following relation [62]

$$\tan \delta = \frac{\epsilon_i}{\epsilon_r}, \quad (8)$$

where $\epsilon_r = n^2 - \kappa^2$ and $\epsilon_i = 2n\kappa$.

It is found from Fig. 14(a) that the loss factor increases with increase of photon energy. The films with high Nb concentration has high loss factor compared to the undoped film.

The rate of energy loss of electrons as they traverse the bulk or the surface are measured in terms of the volume energy loss function (VELF) and surface energy loss function (SELF) [64]. VELF and SELF are related to the optical properties of the material via the real and imaginary parts of the dielectric constant by the following relations [65].

$$VELF = \frac{\epsilon_i}{\epsilon_r^2 + \epsilon_i^2} \quad (9)$$

$$SELF = \frac{\epsilon_i}{(\epsilon_r + 1)^2 + \epsilon_i^2}. \quad (10)$$

The VELF and SELF of all the films show similar behaviour (Fig. 14(b) and 14(c)). The values of VELF and SELF increase with increasing photon energy. Also the values of VELF are higher than that of SELF at higher energy. The films with low Nb concentration have lower values of VELF and SELF compared to the films with higher doping concentration.

The thickness of the films is also determined from spectroscopic ellipsometry. Good agreement has been obtained between the film thickness values determined using spectroscopic ellipsometry and cross sectional FESEM images (Table 2).

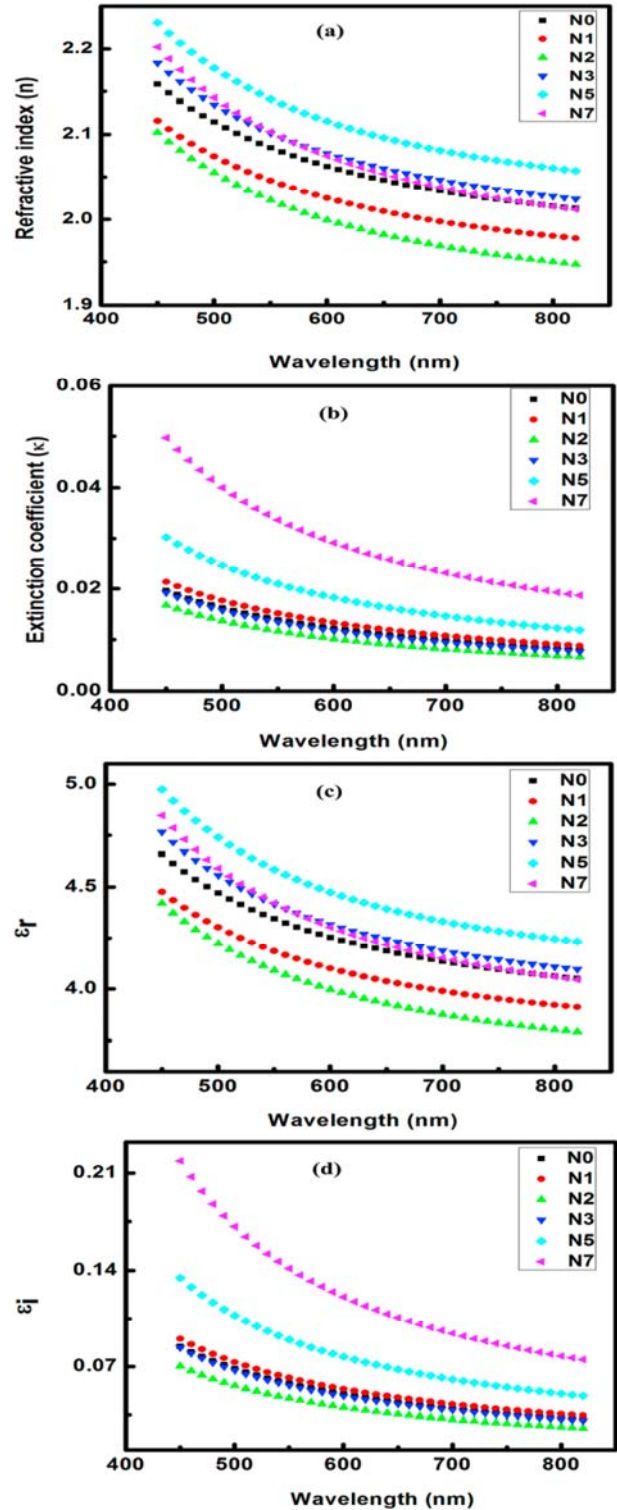


Figure 13 Variation of (a) refractive index (n), (b) extinction coefficient (κ), (c) real part of dielectric constant (ϵ_r) and (d) imaginary part of dielectric constant (ϵ_i) of Nb doped In_2O_3 films with wavelength by ellipsometry.

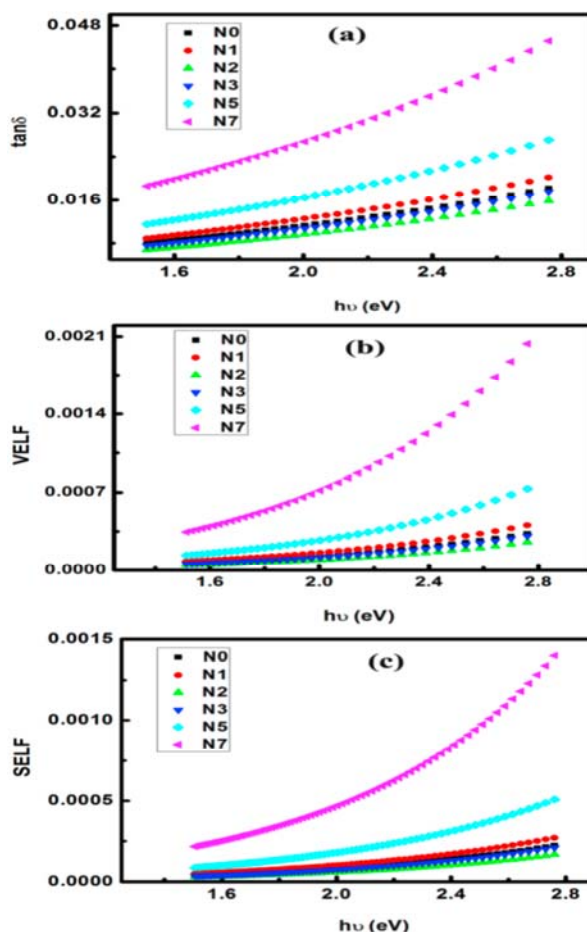
Table 4 Optical parameters of undoped and Nb doped In_2O_3 films deposited by RF magnetron sputtering.

Sample code	χ^2	Optical constants using spectroscopic ellipsometry		Average transmittance in the 400–900 nm region (%)	Band gap energy (eV)
		Refractive index (n)	Extinction coefficient (κ)		
N0	0.16	2.08	0.014	81	3.56
N1	0.13	2.04	0.015	86	3.64
N2	0.06	2.02	0.012	84	3.64
N3	0.54	2.10	0.013	84	3.65
N5	0.83	2.14	0.020	84	3.69
N7	0.28	2.10	0.034	86	3.65

5.3 Photoluminescence analysis The effect of Nb on the luminescence properties of In_2O_3 films is studied using photoluminescence (PL) spectroscopy. It is reported that bulk In_2O_3 cannot emit light at room temperature while films and nanostructures of indium oxide give emission in the UV and visible region [66, 67].

Figure 15 shows the room temperature photoluminescence spectra of as-deposited undoped and Nb doped In_2O_3 films recorded using an excitation radiation of wavelength 250 nm. The PL spectrum of the undoped In_2O_3 film (Fig. 15(a)) shows a very intense broad UV emission at 397 nm with a shoulder peak at ~ 341 nm and an intense emission at 469 nm. The PL spectra of the Nb doped films (Fig. 15(b)) except that of the N3 film presents two intense bands at 366 nm and 469 nm. The PL spectrum of the N3 film shows emissions at 352 nm and 429 nm with reduced intensity. The intensity of the PL emission in the Nb doped films are much less compared to the undoped film and the N3 film shows the lowest PL intensity.

Dai et al. [68] reported emissions at 392 nm and 468 nm in In_2O_3 nanowires synthesized by chemical route. They have attributed the blue emission to the existence of oxygen vacancies and UV emission to the recombination from the localized defect states or the quantum size effect of nanowires. In pulsed laser ablated In_2O_3 thin films, Beena et al., reported two intense broad PL emissions ~ 286 nm and 390 nm region [61]. Strong and broad PL emission peaks centered at 470 nm has been reported in In_2O_3 nanofibers [69] and nanowires [70]. Zheng et al. reported strong PL emission peaks centered at 425, 429, 442 and 460 nm in In_2O_3 nanowires synthesized by the EDO method [71]. Blue emissions at 416 and 435 nm have been reported by Wu et al. for In_2O_3 nanowires prepared by carbothermal reduction approach [72].

**Figure 14** Variation of (a) loss factor, (b) volume energy loss, and (c) surface energy loss for undoped and Nb doped In_2O_3 films as a function of photon energy.

The synthesized In_2O_3 films can have defects such as oxygen vacancy, indium vacancy, oxygen interstitials, indium interstitials, stacking faults etc. [73]. These defects would induce the formation of new energy levels in the band gap. The intense UV emission observed in the present case can be assigned to the transition of electrons from the oxygen vacancy energy level near the electron band edge to the valence band [74]. The visible emission from the Nb doped In_2O_3 films can be attributed to the defect related deep-level emission [75].

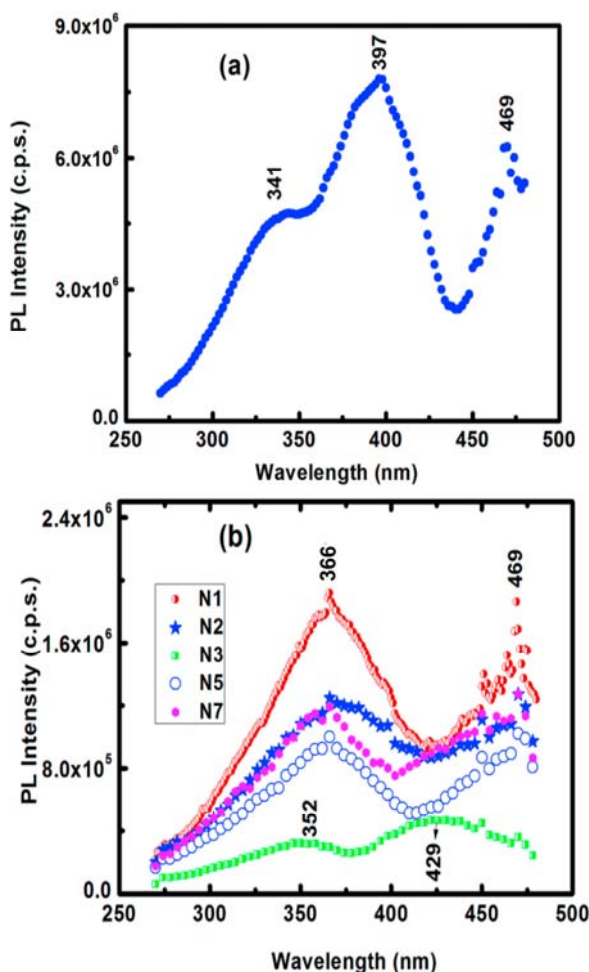


Figure 15 Photoluminescence (PL) spectra of RF sputtered as-deposited (a) undoped In_2O_3 film and (b) Nb doped In_2O_3 films recorded using an excitation wavelength of 250 nm.

The observed enhancement in the PL intensity for the undoped film compared to the doped films can be due to the presence of excess oxygen deficiency and bigger crystallites in it. Increased oxygen deficiency concentration is also suggested by the minimum resistivity shown by the undoped film. Bigger crystallites reduce the grain boundary density which in turn decreases the scattering of light [76].

6 Electrical studies The electrical parameters obtained from the Hall-effect measurements of as-deposited undoped and Nb doped In_2O_3 films with doping concentration 3, 5 and 7 wt% are shown in Table 5. All the films show n-type semiconducting behaviour as electrons are the prominent type of carriers. The undoped In_2O_3 film possesses a carrier concentration of $3.49 \times 10^{19} \text{ cm}^{-3}$. This high concentration of carriers in the undoped film can be due to inherent defects in the film [28]. All the films have carrier concentration of the order of 10^{19} cm^{-3} . Doping Nb into In_2O_3 lattice improves the mobility of the charge carriers. The undoped In_2O_3 film has carrier mobility $8.6 \text{ cm}^2 \text{ V}^{-1} \text{ s}^{-1}$ and for the N5 film it is $16.8 \text{ cm}^2 \text{ V}^{-1} \text{ s}^{-1}$.

The undoped film shows an electrical resistivity of $2.08 \times 10^{-2} \Omega \text{ cm}$. As the Nb doping concentration is increased, the carrier concentration slightly decreases. Thus there can be a reduction in the density of scattering centers thereby increasing the mobility [77]. The decrease in the carrier concentration observed with Nb doping can be related to the reduction in crystallinity as revealed by XRD analysis [78]. This can reduce the conductivity of the doped films. The electrical properties of the undoped In_2O_3 and Nb doped In_2O_3 films prepared in the present case are compared with the reported values of Nb doped In_2O_3 films and other TCOs and the results are presented in Table 6.

Table 5 Electrical parameters of as-deposited undoped film N0 and Nb doped In_2O_3 films N3, N5, N7.

Sample code	Carrier concentration (cm^{-3})	Electrical resistivity ($\Omega \text{ cm}$)	Mobility ($\text{cm}^2 \text{ V}^{-1} \text{ s}^{-1}$)	Carrier type
N0	3.49×10^{19}	2.08×10^{-2}	8.61	n
N3	1.08×10^{19}	3.78×10^{-2}	15.3	n
N5	1.07×10^{19}	3.48×10^{-2}	16.8	n
N7	1.23×10^{19}	3.15×10^{-2}	16.1	n

Table 6 Comparison of the electrical properties of reported Nb doped In_2O_3 films and some transparent conducting oxide films with the present study.

TCO	Method of preparation	Deposition/annealing temperature (°C)	Carrier concentration (cm^{-3})	Hall mobility ($\text{cm}^2\text{V}^{-1}\text{s}^{-1}$)	Resistivity (Ωcm)	Reference
In_2O_3 film	RF magnetron sputtering	Room temp.	3.49×10^{19}	8.61	2.08×10^{-2}	Present work
Nb: In_2O_3 film	„	„	1.07×10^{19}	16.8	3.48×10^{-2}	Present work
Nb: In_2O_3 film	sol-gel technique	500 °C			1.19×10^{-1}	[21]
Nb: In_2O_3 film	Pulsed laser deposition	Room temp.		15	$\sim 10^{-3}$	[25]
Nb: In_2O_3 film	„	600 °C		85	9.16×10^{-5}	[25]
Nb: In_2O_3 film	„		1.3×10^{21}	65	9.61×10^{-5}	[26]
Nb: In_2O_3 film	Co-sputtering	550 °C	0.87×10^{21}	17.4	4.1×10^{-4}	[28]
Nb:ITO films	„	600 °C	4.8×10^{20}	45.4	3.15×10^{-4}	[24]
Nb:ITO films	sol-gel technique	500 °C			3.72×10^{-2}	[79]
Nb:ITO films	RF magnetron sputtering	Room temp.	1.36×10^{21}	17.6	3.10×10^{-4}	[80]
Al:ZnO films (AZO)	„	„	0.86×10^{21}	15.6	4.62×10^{-4}	[81]
F:SnO ₂ films (FTO)	„	300 °C	2.02×10^{20}	19	1.63×10^{-3}	[82]
ITO films	DC magnetron sputtering	350 °C	1.89×10^{21}	19	1.28×10^{-4}	[83]
	RF magnetron sputtering		1.46×10^{21}	32.7	1.29×10^{-4}	

7 Conclusions The influence of Nb on the structural, morphological, optical and electrical properties of In_2O_3 films is studied. The as-deposited In_2O_3 and Nb doped In_2O_3 films present polycrystalline nature showing cubic-bixbyite structure. Moderate doping of Nb enhances the crystalline quality of the In_2O_3 films where as heavy doping results in the decline of its crystalline quality. The average size of the crystallites decreases systematically with Nb concentration. Micro-Raman analysis shows the presence of characteristic bands of In_2O_3 cubic bixbyite phase in the films. XPS analysis reveals the presence of Nb^{4+} in the Nb doped film. AFM and FESEM analysis presents a smooth surface morphology with uniform dense distribution of smaller grains for both undoped and doped films. EDS and XPS analysis shows the incorporation of Nb in the doped films. Good agreement has been achieved by the thickness calculation using ellipsometry and cross sectional SEM analysis. Spectroscopic ellipsometry analysis reveals that the value of refractive index, extinction coefficient,

real and imaginary parts of dielectric constant shows normal dispersion behaviour. Both the undoped and doped films show very high transmittance. All films exhibit a bright photoluminescence emission in the UV and visible regions. The Hall effect measurements shows high value of mobility for the Nb doped films compared to the undoped In_2O_3 film. The Nb doped In_2O_3 films present good crystalline quality, smooth surface morphology, high transparency, good electrical and optical properties and intense photoluminescence emission. This shows the suitability of Nb doped In_2O_3 films for optoelectronic applications.

References

- [1] A. Stadler, *Materials* **5**, 661 (2012).
- [2] H. Liu, V. Avrutin, N. Izyumskaya, Ü. Özgür, and H. Morkoç, *Superlattices Microstruct.* **48**, 458 (2010).
- [3] D. S. Ginley, H. Hosono, and D. C. Paine, *Handbook of Transparent Conductors* (Springer Science and Business Media, New York, 2010), p. 1.

- [4] D. Liu, W. W. Lei, B. Zou, S. D. Yu, J. Hao, K. Wang, B. B. Liu, Q. L. Cui, and G. T. Zou, *J. Appl. Phys.* **104**, 083506 (2008).
- [5] P. Prathap, G. G. Devi, Y. P. V. Subbaiah, K. T. R. Reddy, and V. Ganesan, *Curr. Appl. Phys.* **8**, 120 (2008).
- [6] E. Savarimuthu, K. C. Lalithambika, A. M. E. Raj, L. C. Nehru, S. Ramamurthy, A. Thayumanavan, C. Sanjeeviraja, and M. Jayachandra, *J. Phys. Chem. Solids* **68**, 1380 (2007).
- [7] K. Sreenivas, T. S. Rao, A. Mansingh, and S. Chandra, *J. Appl. Phys.* **57**, 384 (1985).
- [8] Y. Shigesato, S. Thalaki, and T. Haranoh, *J. Appl. Phys.* **71**, 3356 (1992).
- [9] A. Murali, A. Barve, V. J. Leppert, S. H. Risbud, I. M. Kennedy, and H. W. H. Lee, *Nano Lett.* **1**, 287 (2001).
- [10] Z. Fang, H. Assaoudi, R. I. L. Guthrie, J. A. Kozinski, and I. S. Butler, *J. Am. Ceram. Soc.* **90**, 2367 (2007).
- [11] Hamberg and C. G. Granqvist, *J. Appl. Phys.* **60**, R123 (1986).
- [12] E. Li, Z. Cheng, J. Xu, Q. Pan, W. Yu, and Y. Chu, *Cryst. Growth Des.* **9**, 2146 (2009).
- [13] S. Elouali, L. G. Bloor, R. Binions, I. P. Parkin, C. J. Carmalt, and J. A. Darr, *Langmuir* **28**, 1879 (2012).
- [14] S. Shanmugan and D. Mutharasu, *Metall. Mater. Trans. A* **43**, 6 (2012).
- [15] H. A. Mohamed, *Int. J. Phys. Sci.* **7**(13), 2102 (2012).
- [16] N. W. Pu, W. S. Liu, H. M. Cheng, H. C. Hu, W. T. Hsieh, H. W. Yu, and S. C. Liang, *Materials* **8**, 6471 (2015).
- [17] S. Parthiban, V. Gokulakrishnan, K. Ramamurthi, E. Elangovan, R. Martins, E. Fortunato, and R. Ganesan, *Sol. Energy Mater. Sol. Cells* **93**, 92 (2009).
- [18] D. Beena, R. Vinodkumar, I. Navas, V. Ganesan, A. Yamuna, and V. P. M. Pillai, *J. Alloys Compd.* **539**, 63 (2012).
- [19] R. K. Gupta, K. Ghosh, S. R. Mishra, and P. K. Kahol, *Appl. Surf. Sci.* **253**, 9422 (2007).
- [20] L. T. Yan and R. E. I. Schropp, *Thin Solid Films* **520**, 2096 (2012).
- [21] S. Mohammadi, M. R. Golobostanfard, and H. Abdizadeh, *J. Mater. Sci. Technol.* **29**, 923 (2013).
- [22] B. N. Joshi, H. Yoon, M. F. A. M. van Hest, and S. S. Yoon, *J. Am. Ceram. Soc.* **96**, 2623 (2013).
- [23] A. Singhal, S. N. Achary, J. Manjanna, O. D. Jayakumar, R. M. Kadam, and A. K. Tyagi, *J. Phys. Chem. C* **113**, 3600 (2009).
- [24] J. H. Kim, T. Y. Seong, S. I. Na, K. B. Chung, H. M. Lee, and H. K. Kim, *J. Vac. Sci. Technol. A* **32**, 021202 (2014).
- [25] R. K. Gupta, K. Ghosh, R. Patel, and P. K. Kahol, *J. Cryst. Growth* **310**, 4336 (2008).
- [26] R. K. Gupta, K. Ghosh, R. Patel, S. R. Mishra, and P. K. Kahol, *Mater. Chem. Phys.* **112**, 136 (2008).
- [27] O. Lozano, Consequences of Nb-doping to In_2O_3 : A Magneto-transport and Optical Study of a Novel Thin Film Transparent Conductor, PhD. thesis, University of Houston, 2009.
- [28] O. Lozano, Q. Y. Chen, P. V. Wadekar, H. W. Seo, P. V. Chinta, L. H. Chu, L. W. Tu, I. Lo, S. W. Yeh, N. J. Ho, F. C. Chuang, D. J. Jang, D. Wijesundera, and W. K. Chu, *Sol. Energy Mater. Sol. Cells* **113**, 171 (2013).
- [29] M. G. S. Paz and R. R. Bon, *Thin Solid Films* **517**, 2596 (2009).
- [30] Y. S. Jung, J. Y. Seo, D. W. Lee, and D. Y. Jeon, *Thin Solid Films* **445**, 63 (2003).
- [31] M. Bender, N. Katsarakis, E. Gagaoudakis, E. Hourdakis, E. Douloufakis, V. Cimalla, and G. Kiriakidis, *J. Appl. Phys.* **90**, 5382 (2001).
- [32] B. D. Cullity, *Elements of X-ray Diffraction* (Addison-Wesley Publishing Co., Inc., Massachusetts, 1956), p. 99.
- [33] G. K. Williamson and W. H. Hall, *Acta Metall.* **1**, 22 (1953).
- [34] W. G. Fateley, F. R. Dollish, N. T. Mc Devitt, and F. B. Freeman, *Infrared and Raman Selection Rules for Molecular and Lattice Vibrations: The correlation Method* (Wiley-Interscience, New York, 1972), pp. 178, 212.
- [35] R. R. Krishnan, R. S. Sreedharan, S. K. Sudheer, C. Sudarasanakumar, V. Ganesan, P. Srinivasan, and V. P. M. Pillai, *Mater. Sci. Semicond. Process* **37**, 112 (2015).
- [36] J. Gan, X. Lu, J. Wu, S. Xie, T. Zhai, M. Yu, Z. Zhang, Y. Mao, S. C. I. Wang, Y. Shen, and Y. Tong, *Sci. Rep.* **3**, 1021 (2013).
- [37] M. Kaur, N. Jain, K. Sharma, S. Bhattacharya, M. Roy, A. K. Tyagi, S. K. Gupta, and J. V. Yakhmi, *Sens. Actuators B* **133**, 456 (2008).
- [38] Q. Williams, R. J. Hemley, M. B. Kruger, and R. Jeanloz, *J. Geophys. Res.* **98**, 22157 (1993).
- [39] M. J. Procop, *Electron Spectrosc. Relat. Phenom.* **59**, R1 (1992) [NIST XPS Database: <http://srdata.nist.gov/xps/>].
- [40] S. K. Vishwanath, K. Y. Cho, and J. Kim, *J. Phys. D: Appl. Phys.* **49**, 155501 (2016).
- [41] M. C. Nguyen, M. Jang, D. H. Lee, H. J. Bang, M. Lee, J. K. Jeong, H. Yang, and R. Choi, *Sci. Rep.* **6**, 25079 (2016).
- [42] J. C. C. Fan and J. B. Goodenough, *J. Appl. Phys.* **48**, 3524 (1977).
- [43] J. P. Bonnelle, J. Grimblot, and A. D'Huysser, *J. Electron. Spectrosc.* **7**, 151 (1975).
- [44] K. K. Banger, Y. Yamashita, K. Mori, R. L. Peterson, T. Leedham, J. Rickard, and H. Sirringhaus, *Nature Mater.* **10**, 45 (2011).
- [45] Y. An, S. Wang, L. Duan, J. Liu, and Zhonghua Wu, *Appl. Phys. Lett.* **102**, 212411-1 (2013).
- [46] A. L. Viet, M. V. Reddy, R. Jose, B. V. R. Chowdari, and S. Ramakrishna, *J. Phys. Chem. C* **114**, 664 (2010).
- [47] M. Naeem, S. Qaseem, I. Ahmad, and M. Maqbool, *J. Nanopart. Res.* **14**, 1(2012).
- [48] V. Luhn, I. Zharsky, and P. Zhukowski, *Acta Phys. Pol.* **A 123**, 837 (2013).
- [49] G. C. Park, S. M. Hwang, S. M. Lee, J. H. Choi, K. M. Song, H. Y. Kim, H. S. Kim, S. J. Eum, S. B. Jung, J. H. Lim, and J. Joo, *Sci. Rep.* **5**, 10410 (2015).
- [50] I. Horcas, R. Fernández, J. M. G. Rodríguez, J. Colchero, J. G. Herrero, and A. M. Baro, *Rev. Sci. Instrum.* **78**, 013705 (2007).
- [51] R. J. Bose, R. Vinodkumar, S. K. Sudheer, V. R. Reddy, V. Ganesan, and V. P. M. Pillai, *J. Appl. Phys.* **112**, 114311 (2012).
- [52] K. J. Lethy, D. Beena, R. Vinodkumar, V. P. M. Pillai, V. Ganesan, and V. Sathe, *Appl. Surf. Sci.* **254**, 2369 (2008).
- [53] J. I. Pankove, *Optical Processes in Semiconductors* (Dover Publications, Inc., New York, 1971), p. 35.

- [54] D. Beena, K.J. Lethy, R. Vinodkumar, V.P. M. Pillai, V. Ganesan, D.M. Phase, and S.K. Sudheer, *Appl. Surf. Sci.* **255**, 8334 (2009).
- [55] M. Suche, S. Christoulakis, M. Katharakis, N. Vidakis, and E. Koudoumas, *Thin Solid Films* **517**, 4303 (2009).
- [56] R. J. Bose, V.S. Kavitha, C. Sudarsanakumar, and V.P. M. Pillai, *Appl. Surf. Sci.* **379**, 505 (2016).
- [57] J. Lv, K. Huang, X. Chen, J. Zhu, C. Cao, X. Song, and Z. Sun, *Opt. Commun.* **284**, 2905 (2011).
- [58] O. V. Overschelde, G. Guisbiers, F. Hamadi, A. Hemberg, R. Snyders, and M. Wautelet, *J. Appl. Phys.* **104**, 103106 (2008).
- [59] T. Gerfina and M. Gratzel, *J. Appl. Phys.* **79**, 1722 (1996).
- [60] F. O. Adurodija, L. Semple, and R. Bruning, *Thin Solid Films* **492**, 153 (2005).
- [61] D. Beena, R. Vinodkumar, I. Navas, G. Rajanand, and V. P. Mahadevan Pillai, *Mater. Sci. Eng. B* **174**, 59 (2010).
- [62] R. Vinodkumar, I. Navas, K. Porsezian, V. Ganesan, N.V. Unnikrishnan, and V. P. Mahadevan Pillai, *Spectrochim. Acta A* **118**, 724 (2014).
- [63] A. A. Al-Ghamdi, W.E. Mahmoud, S.J. Yaghmour, and F.M. Al-Marzouki, *J. Alloys Compd.* **486**, 9 (2009).
- [64] A. S. Gadallah and M.M. El-Nahass, *Adv. Condens. Matter Phys.* **2013**, ID 234546 (2013).
- [65] A. M. Salem, *Appl. Phys. A* **74**, 205 (2002).
- [66] J. Gao, R. Chen, D. H. Li, L. Jiang, J. C. Ye, X. C. Ma, X. D. Chen, Q. H. Xiong, H. D. Sun, and T. Wu, *Nanotechnology* **22**, 195706 (2011).
- [67] Q. Tang, W. Zhou, W. Zhang, S. Ou, K. Jiang, W. Yu, Y. Qian, *Cryst. Growth Des.* **5**, 147 (2005).
- [68] L. Dai, X. L. Chen, J. K. Jian, M. He, T. Zhou, and B. Q. Hu, *Appl. Phys. A* **75**, 687 (2002).
- [69] X. S. Peng, G. W. Meng, X. F. Wang, Y. W. Wang, J. Zhang, X. Liu, and L. D. Zhang, *Chem. Mater.* **14**, 4490 (2002).
- [70] C. Liang, G. Meng, Y. Lei, F. Phillipp, and L. Zhang, *Adv. Mater.* **13**, 1330 (2001).
- [71] M. J. Zheng, L. D. Zhang, G. H. Li, X. Y. Zhang, and X. F. Wang, *Appl. Phys. Lett.* **79**, 839 (2001).
- [72] X. C. Wu, J. M. Hong, Z. J. Han, and Y. R. Tao, *Chem. Phys. Lett.* **373**, 28 (2003).
- [73] T. Tomita, K. Yamashita, Y. Hayafuji, and H. Adachi, *Appl. Phys. Lett.* **87**, 051911-1 (2005).
- [74] C. L. Hsin, J. H. He, and L. J. Chen, *Appl. Phys. Lett.* **88**, 063111-1 (2006).
- [75] P. Wu, Q. Li, C. X. Zhao, D. L. Zhang, L. F. Chi, and T. Xiao, *Appl. Surf. Sci.* **255**, 3201 (2008).
- [76] G. Rajan, K. G. Gopchandran, *J. Optoelectron. Adv. Mater.* **11**, 590 (2009).
- [77] B. Kumar, H. Gong, and R. Akkipeddi, *J. Appl. Phys.* **97**, 063706 (2005).
- [78] L.R.O. Cruz and O.J. Santos, *Mater. Lett.* **12**, 72 (1991).
- [79] S. Mohammadi, H. Abdizade, and M. Reza Golobostanfard, *Ceram. Int.* **39**, 4391 (2013).
- [80] S.-N. Li, R.-X. Ma, C.-H. Ma, D.-R. Li, Y.-Q. Xiao, L.-W. He, and H.-M. Zhu, *Optoelectron. Lett.* **9**, 0198 (2013).
- [81] W. Yang, Z. Liu, D.L. Peng, F. Zhang, H. Huang, Y. Xie, and Z. Wu, *Appl. Surf. Sci.* **255**, 5669 (2009).
- [82] B. H. Liao, C. C. Kuo, P. J. Chen, and C. C. Lee, *Appl. Opt.* **50**, C106 (2011).
- [83] O. Tuna, Y. Selamet, G. Aygun, and L. Ozyuzer, *J. Phys. D: Appl. Phys.* **43**, 055402-1 (2010).